Formation of nanocrystalline films of Sr_2FeMoO_6 on Si(100) by pulsed laser deposition: Observation of preferential oriented growth

Helia Jalili,[1] Nina F. Heinig,[2] and K. T. Leung[1,2,a)]
[1]*Department of Physics, University of Waterloo, Waterloo, Ontario N2L 3G1, Canada*
[2]*Department of Chemistry, University of Waterloo, Waterloo, Ontario N2L 3G1, Canada*

(Received 16 June 2008; accepted 16 December 2008; published online 5 February 2009)

Nanocrystalline Sr_2FeMoO_6 films have been grown on a Si(100) substrate by pulsed laser deposition under different growth conditions including deposition temperature and time. A nanocrystalline single-phase Sr_2FeMoO_6 film was obtained at a temperature as low as 600 °C. This high-quality ferromagnetic film was found to have a saturation magnetic moment of $3.4\mu_B$ per formula unit and a coercive field of 1.5 kOe at 77 K with micrometer-sized magnetic domains. By using glancing-incidence x-ray diffraction with different incident beam angles, the crystal structure of the film was sampled as a function of depth. For the as-grown Sr_2FeMoO_6 films thicker than 60 nm, a preferential orientation of the nanocrystals in the film was observed, despite the lack of good lattice matching with the Si substrate. At a higher deposition temperature of 800 °C, the as-grown film exhibited the same saturation magnetic moment but with a discernibly lower coercive field of 0.8 kOe, consistent with the larger grain size obtained at a higher growth temperature. © *2009 American Institute of Physics*. [DOI: 10.1063/1.3073897]

I. INTRODUCTION

Half-metallic ferromagnets are important in spin-based electronic devices and potentially in the data storage industry. In half-metallic ferromagnetic materials, the densities of states at the Fermi level are unbalanced. The spin-polarized characteristics of these materials make them promising candidates to be used as spin sources in devices such as spin valves and magnetic tunnel junctions. Among all spin-polarized materials, those with Curie temperatures (T_C) higher than room temperature are generally more desirable for device applications.[1–3]

As a well known conducting ferromagnet (or ferrimagnet) with a relatively high T_C of 410–450 K,[4] the double perovskite Sr_2FeMoO_6 is one of these promising candidate materials. In 1998, Kobayashi *et al.*[5] demonstrated the low-field magnetoresistant response of Sr_2FeMoO_6 at room temperature, drawing attention to the spin and electronic properties of this type of double perovskite materials. Their electronic structure calculations further showed that ordered Sr_2FeMoO_6 is half metallic and it exhibits tunneling-type magnetoresistance (MR) at room temperature. In Sr_2FeMoO_6, the crystal structure is tetragonal[4] with each of Fe and Mo surrounded by six O atoms. The magnetic structure has been described as an ordered arrangement of Fe^{3+} ($3d^5$, $S=5/2$) magnetic moments antiferromagnetically coupled to the Mo^{5+} ($4d^1$, $S=1/2$) moments, resulting in a total saturation magnetic moment of $4\mu_B$ at low temperature. However, most experimental results to date reported a saturation magnetic moment less than this expected value.[6–10]

One possible explanation for this discrepancy is the presence of antisite defects. When the Fe^{3+} cation is misplaced with the Mo^{5+} cation, an antisite defect is formed and it changes the transport and magnetic properties of the resulting material. Experimental results by Navarro *et al.*[11] showed that the presence of antisite defects lowers the saturation magnetic moment and T_C values. Furthermore, Monte Carlo calculations by Ogale *et al.*[12] illustrated that both the saturation magnetic moment and T_C of these materials are strongly dependent on the antisite defect density, and that the oxygen content could also play an important role in the magnitude of the magnetic moment, especially in samples with more disorder. Saha-Dasgupta and Sarma[13] used *ab initio* band structure calculations to show that the presence of antisite defects destroys the half-metallic nature of this material and reduces the magnetic moment at the Fe sites.

Another proposal to account for the lower experimental saturation magnetic moment is the presence of grain and antiphase boundaries,[14,15] which has also been used to explain the low-field MR in Sr_2FeMoO_6. It is believed that MR occurs when the electrons tunnel through secondary phases in the grain boundary. Several groups[7,16] measured the MR of polycrystalline samples with different grain sizes and antisite defect densities, and they concluded that both inter- and intragranular effects are responsible for the MR. For Sr_2FeMoO_6 grown on $SrTiO_3$(001) bicrystals, Yin *et al.*[8] attributed the low-field MR to the spin-dependent transfer across grain boundaries and not to an intragranular effect. Later, Niebieskikwiat *et al.*[14] showed that for polycrystalline $Sr_2FeMoO_{6+\delta}$ ($\delta=0.04$) samples the magnetization and lattice parameters were the same as those for Sr_2FeMoO_6, but the MR for the former sample was enhanced, which led them to believe that extra oxygen at the grain boundary region could be responsible for the enhancement.

The magnetic and electronic properties of Sr_2FeMoO_6 greatly depend on the different forms of the samples: single crystal, polycrystalline, or thin film. Preparation conditions and postannealing can significantly affect the physical prop-

a)Author to whom correspondence should be addressed. Electronic mail: tong@uwaterloo.ca.

erties of this material. Pulsed laser deposition (PLD) has been commonly used to grow epitaxial single-crystal Sr_2FeMoO_6 samples mostly on $SrTiO_3(100)$ substrates due to their good lattice match,[8–10,17] while solid-state synthesis is one of the most common methods for growing polycrystalline Sr_2FeMoO_6 samples.[14,15] Magnetron sputtering[18] and wet-chemistry methods[7,19] could also be used to produce single-crystal film and bulk polycrystalline samples, respectively. However, the deposition temperatures in almost all of the reported cases were higher than 800 °C. Furthermore, many of the reported samples have been postannealed at even higher temperatures. For applications in the microelectronic industry, where silicon is the most widely used and therefore desirable substrate for fabricating integrated devices, a lower deposition temperature is generally preferred. In the present work, single-phase polycrystalline Sr_2FeMoO_6 has been grown on Si(100) for the first time by using the PLD method. Furthermore, by changing the growth temperature, we have been able to control the grain size of the Sr_2FeMoO_6 sample. Good quality samples, as determined by x-ray diffraction and magnetization measurements, have been obtained on Si(100) at a growth temperature as low as 600 °C. We also show that despite the lack of lattice matching due to the presence of native oxide, partially oriented growth of nanocrystals in the Sr_2FeMoO_6 film can be achieved on Si(100). The present results open up the prospect of integrating these oriented nanocrystalline Sr_2FeMoO_6 films into Si device fabrication.

II. EXPERIMENTAL DETAILS

A NanoPLD system (PVD Products) with a base pressure better than 5×10^{-7} torr was used for the film growth experiments. The system was equipped with a KrF excimer laser with a maximum laser fluence of 600 mJ/pulse. The Si(100) substrates (99.99% purity, Waferworld), 10 $\times$10 mm^2 in size, were mounted on the substrate holder. The 1 in. diameter Sr_2FeMoO_6 target (99.95% purity) was obtained commercially (from MTI). With the target-to-substrate distance set to 42 mm, thin films were deposited on the Si substrates in vacuum (with no additional oxygen) for a preselected period of time with the substrates held at a fixed temperature between 400 and 800 °C. A laser fluence of 400 mJ/pulse was used and the repetition rate was set to 10 Hz.

For each growth condition, the morphology of the resulting film was characterized by field-emission scanning electron microscopy (SEM) (LEO 1530) and atomic force microscopy (AFM) (DI Nanoscope IV) operated in a tapping mode. For selected growth conditions, the film thicknesses were determined by lift-off lithography using silver paste and AFM imaging. The local magnetic moments were measured by magnetic field microscopy (MFM) using a Co–Cr tip. The total magnetic moment was measured by using a superconducting quantum interference device (SQUID) magnetometer (Quantum Design). The structure of the film was analyzed by glancing-incidence x-ray diffraction (GIXRD) in a PANalytical X'Pert Pro MRD system, equipped with an x-ray mirror as the incident beam optics and a parallel plate collimator as the diffracted beam optics.

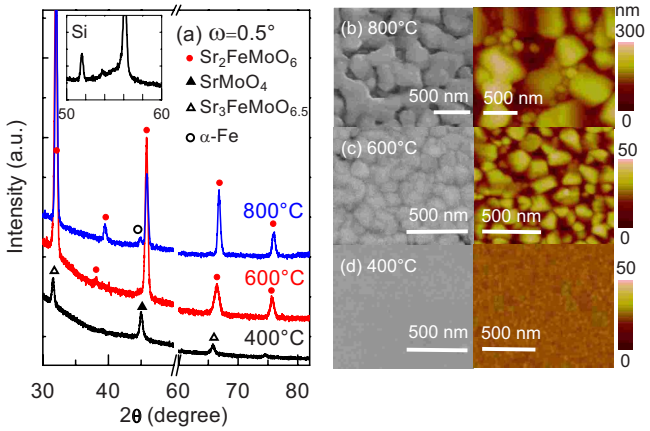

FIG. 1. (Color online) GIXRD spectra recorded at incident angle ω=0.5° (left column), SEM (center column), and AFM images (right column) for samples grown on Si(100) with a laser fluence of 400 mJ/pulse for 30 min at [(a) and (b)] 800 °C, [(a) and (c)] 600 °C, and [(a) and (d)] 400 °C. Features corresponding to Sr_2FeMoO_6 (Ref. 21), $SrMoO_4$ (Ref. 22), α-Fe (Ref. 23), and a rarely observed $Sr_3FeMoO_{6.5}$ phase (Ref. 24) are identified by solid circles (●), solid triangles (▲), open circles (○), and open triangles (△), respectively. For the AFM images (b), (c), and (d), the respective rms roughness parameters are 34.3, 6.9, and 1.8 nm.

GIXRD is a surface sensitive technique useful for studying the crystal structure of surfaces and thin films.[20] The geometry of this diffraction process preferentially probes the surface and near-surface region of a film, allowing detection of a much smaller amount of material than is possible with a conventional powder scan. In GIXRD, the incident x-ray beam is fixed at a small angle of ω near ω_C, where ω_C is the critical angle for total reflection. When the x-ray beam hits the surface at a small incident angle, a part of the beam is reflected. If $\omega<\omega_C$, a part of the incident beam becomes evanescent, propagating parallel to the surface with a penetration depth of a few nanometers. On increasing ω, a part of the beam becomes refracted and the penetration depth increases to a few hundred nanometers. This portion of the x ray (both evanescent and refracted) can be diffracted by the sample and can be measured by scanning 2θ.

III. RESULTS AND DISCUSSION

A. Effect of growth temperature on the crystal structure and magnetic properties

Figure 1(a) shows the GIXRD data collected at an incidence angle ω=0.5° for the films grown on Si(100) at three different temperatures. For a laser fluence of 400 mJ/pulse [4–5 J/cm^2] and a deposition time of 30 min, the resulting film thicknesses are estimated to be 114 nm. The laser energy density reported here was measured on the target surface. We have noticed phase separation of the Sr_2FeMoO_6 for higher laser fluences of 550 mJ/pulse [6–7 J/cm^2]. Phase separation at higher laser densities was also observed by Di Trolio *et al.*[9] on Sr_2FeMoO_6 grown on $SrTiO_3$. For the sample grown at 800 °C, we observe a series of peaks at 2θ =32.0°, 39.5°, 45.8°, 66.8°, and 76.0° [identified by ● in Fig. 1(a)], corresponding respectively to the (112), (202), (004), (224), and (116) planes of Sr_2FeMoO_6,[21] and a small feature at 2θ=44.6° [identified by ○ in Fig. 1(a)] that is

attributed to the (110) plane of α-Fe.[23] The presence of metallic iron has been observed previously by Besse *et al.*[17] in a PLD-grown Sr_2FeMoO_6 film on a $SrTiO_3$ substrate at 856 °C. In the Sr_2FeMoO_6 sample grown at 800 °C, the magnitude of the (110) α-Fe peak corresponds to 1%–2% metallic Fe by volume in the film. For the sample grown at 600 °C [Fig. 1(a)], the α-Fe feature is not evident and only single-phase Sr_2FeMoO_6 is observed. The region between $2\theta=50-60°$ [shown for a bare Si substrate in the inset of Fig. 1(a)] is omitted for the films because the intense features due to the Si substrate could obscure the contributions from the films.[25] Unlike the Sr_2FeMoO_6 films, the GIXRD contribution from the Si substrate is also extremely sensitive to small rotations in the film plane. The prominent peak at $2\theta=45.0°$ observed for the sample grown at 400 °C [identified by ▲ in Fig. 1(a)] can be assigned to the (204) plane of $SrMoO_4$.[22] Upon searching the Powder Diffraction File database, the remaining two peaks at $2\theta=31.4°$ and 65.6° [denoted by △ in Fig. 1(a)] can be attributed to Sr_xFeMoO_y with the best match being $Sr_3FeMoO_{6.5}$.[24] Evidently, the growth at a lower temperature (400 °C) does not produce the stoichiometric Sr_2FeMoO_6 phase.

The corresponding SEM and AFM images of the Sr_2FeMoO_6 films grown on Si(100) at the respective temperatures are also compared in Fig. 1. The film grown at 400 °C appears to be fairly smooth [Fig. 1(d)] with a root mean square (rms) roughness of 1.8 nm for a 4 μm^2 sampling area as determined by AFM. On the other hand, the largely Sr_2FeMoO_6 films grown at 600 °C [Fig. 1(c)] and 800 °C [Fig. 1(b)] look more granular with rms roughness of 6.9 and 34.3 nm for a 4 μm^2 sampling area, respectively. Accordingly, the average grain size of the film grown at 600 °C [Fig. 1(c)] as estimated by AFM (210 nm) is found to be less than half of that for the film grown at 800 °C [540 nm, Fig. 1(b)]. The morphology of the Sr_2FeMoO_6 film grown at 600 °C in the present work [Fig. 1(c)] is very similar to that obtained by Huang *et al.*[7] using a sol-gel method. Energy dispersive x-ray analysis at 20 kV has also been used to identify the elemental stoichiometry of the as-grown films. In particular, the ratio of the atomic percent of Fe to Mo changes from 0.7 to 1.2 to 0.9 for the films grown at 400, 600, and 800 °C, respectively. This is consistent with the GIXRD results [Fig. 1(a)] that show that the film grown at the lower temperature (400 °C) contains additional Mo-rich crystalline phase such as $SrMoO_4$.

By applying the Scherrer analysis to the prominent diffraction peaks at $2\theta=45.05°$, 45.66°, and 45.88° for the films grown at 400, 600, and 800 °C, respectively, we estimate the respective grain sizes to be 66.2, 68.8, and 172.5 nm, which follow the similar trend of increasing grain size with increasing growth temperature as depicted by the SEM and AFM images (Fig. 1). This is also consistent with the increasing roughness with increasing growth temperature seen with AFM. However, the average grain sizes for the films grown at 800 °C (540 nm) and 600 °C (210 nm), as shown in their respective SEM images [Figs. 1(b) and 1(c)], appear much larger than that obtained by the Scherrer analysis, which suggests that the grains in the SEM and AFM images may consist of multiple nanocrystals and/or contain a substantial

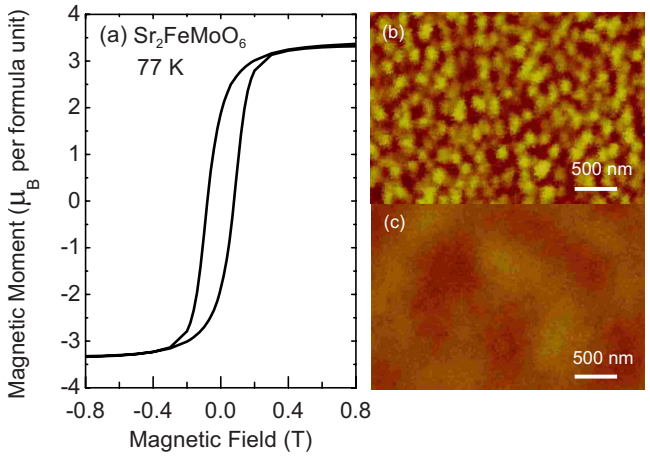

FIG. 2. (Color online) (a) Magnetic moment as a function of applied magnetic field collected at 77 K for the Sr_2FeMoO_6 film grown on Si(100) at 600 °C and the corresponding (b) AFM image and (c) MFM image obtained at a lift height of 30 nm, both collected at room temperature. The height contrast range for the AFM image is 50 nm full scale.

number of defects. On the other hand, for the primary $SrMoO_4$ film obtained at 400 °C, the average grain size as depicted by SEM and AFM appears smaller than that obtained by the Scherrer analysis.

The results shown in Fig. 1 illustrate that a good-quality, single-phase Sr_2FeMoO_6 film can be obtained on a Si substrate at a growth temperature as low as 600 °C. Figure 2(a) shows the corresponding magnetic moment as a function of applied magnetic field up to 5 T, measured at 77 K using a SQUID magnetometer. The magnetic field is applied parallel to the film surface. The diamagnetic contribution from the Si(100) substrate (present as a linear contribution with slope of -6.04×10^{-9} emu/T) has been subtracted from the data. A saturation magnetic moment of $3.4\pm0.1\mu_B$ per formula unit (after appropriate normalization to the film volume) is observed. The corresponding coercive field is found to be 1.5 kOe. For the film grown at 800 °C, we also obtain the same saturation magnetic moment (of $3.4\pm0.1\mu_B$ per formula unit) but a lower coercive field of 0.8 kOe. With 1%–2% of Fe second phase in the film grown at 800 °C, the actual magnetic moment due to Sr_2FeMoO_6 is reduced to $2.8-2.3\mu_B$ per formula unit, as determined by using the analysis of Besse *et al.*[17] The larger coercive field found for the film grown at 600 °C is consistent with the smaller grain size obtained at this lower temperature.

Figures 2(b) and 2(c) show the corresponding AFM and MFM images (taken at room temperature) for the film grown at 600 °C, respectively. In accordance with the SEM image [Fig. 1(c)], the AFM image [Fig. 2(b)] reveals a uniform distribution of regularly shaped grains with an average size of 210 nm. With the magnetic tip magnetized prior to the measurement, several MFM images have been recorded at different lift heights of 30, 50, 80, and 120 nm. All of these MFM images are found to be similar except for the one at 120 nm lift height that shows a very low contrast. A lift height of 30 nm has been used for collecting the MFM image shown in Fig. 2(c), which clearly reveals a ferromagnetic behavior at room temperature. The magnetic domains appear to have an irregular, elongated shape of 0.5×1 μm^2, which

TABLE I. Film thickness, rms roughness and crystal size for Sr_2FeMoO_6 films grown on Si(100) at 600 °C with different deposition times.

Deposition time (min)	Film thickness[a]	rms roughness ±2 (nm)	Crystal size[b] (nm)
1	7	0.8	[c]
10	60	7.6	12.3
20	84	6.6	33.2
30	114	6.9	86.3
60	268	8.1	123.2

[a]The accuracy of the film thickness measurement is ±5 nm.
[b]The average crystal size is obtained by applying the Scherrer analysis to the (004) diffraction line of Sr_2FeMoO_6. The (110) diffraction line of a strain-free *W* target at $2\theta=40.26°$ with FWHM=0.4° has been used as a standard.
[c]For 1 min film, no diffraction lines are observed.

is considerably larger than the grain size (210 nm), indicating that the Sr_2FeMoO_6 grains are well connected electromagnetically. For the samples grown at 400 and 800 °C, we were not able to obtain a MFM image. This is consistent with the lower coercive field for these films as obtained by SQUID magnetometer measurements at 77 K.

B. Effects of deposition time

In order to study the growth evolution of Sr_2FeMoO_6 on Si(100) at 600 °C, we have obtained films for different deposition times of 1, 10, 20, 30, and 60 min. We characterize the morphology of the as-grown films, their respective film thicknesses, and average crystal sizes by using SEM, AFM, and GIXRD, respectively. The growth characteristics of these films are summarized in Table I. Evidently, the corresponding growth rate appears to have stabilized at ~4 nm/min after about 20 min of deposition. The film thicknesses were determined by lift-off lithography and AFM, and while there is some scatter in the data, Table I shows that the film thickness increases linearly with deposition time. The respective SEM and AFM images for the as-grown films shown in Fig. 3 all reveal uniform distributions of grains. The film with the shortest deposition time (1 min) exhibits the smallest grain size with a rms roughness of 0.8 nm over an area of 4 μm^2 [Fig. 3(a)]. Above a deposition time of 10 min, the rms roughness of the thicker film appears to be relatively constant (Table I). For the 60 min film [Fig. 3(e)], a network of cracks is seen to develop over the entire film surface, which may be due to differences in the thermal expansion characteristics between the Si(100) substrate and the thick Sr_2FeMoO_6 film. Furthermore, the average crystal size has been deduced from the full width at half maximum of the (004) peak of Sr_2FeMoO_6 by using the Scherrer analysis. The average crystal size is found to clearly increase with increasing deposition time (Table I).

In addition to providing the average crystal size, GIXRD can also be used to obtain the composition of the crystal phase and orientation as a function of depth by varying the incident angle. This technique has been used to study the residual strain and stress in thin films and to characterize crystalline phases and structures of the near surface in thin films and organic materials.[26–28] The dependence of x-ray

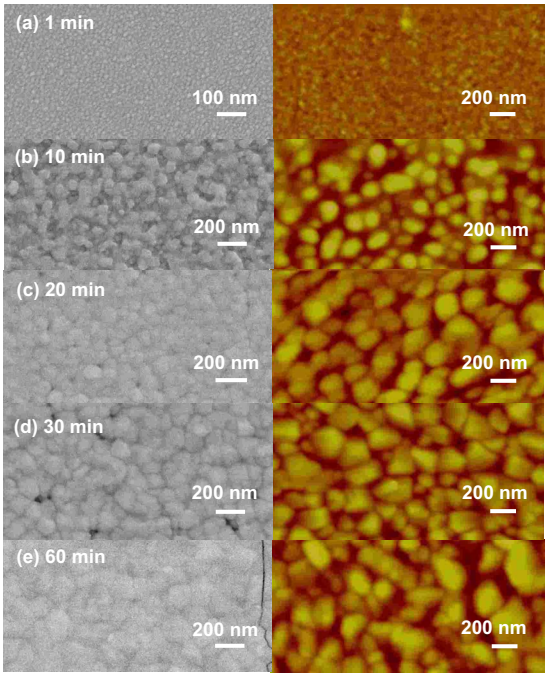

FIG. 3. (Color online) SEM (left) and AFM images (right) of the Sr_2FeMoO_6 films grown on Si(100) at 600 °C with a laser fluence of 4–5 J/cm^2 (400 mJ/pulse) for deposition times of (a) 1, (b) 10, (c) 20, (d) 30, and (e) 60 min. The height contrast range in all the AFM figures is 70 nm, except for the film grown for 1 min shown in (a) with a height contrast range of 10 nm.

$1/e$ penetration depth D as a function of the incident angle ω can be determined by the following equation:

$$D(\omega)=\frac{\lambda}{4\pi}\left(\frac{\sqrt{(\omega^2-\omega_c^2)^2+4\beta^2}+\omega^2-\omega_c^2}{2}\right)^{-(1/2)}, \qquad (1)$$

where λ is the wavelength of the x-ray (1.54 Å for Cu $K\alpha$ radiation), ω_c is the critical angle where total reflection occurs, $\beta=\mu\lambda/(4\pi)$, and μ is the corresponding mass attenuation coefficient (1175 cm^{-1}).[26,27,29] Depending on the material, the typical value for ω_c ranges from 0.2° to 0.6° for Cu $K\alpha$ radiation. $D(\omega)$ has been measured and calculated for different materials[26–28,30] and it generally ranges from a few nanometers for $\omega=0.1°$ to a micrometer for $\omega=1°$. For our Sr_2FeMoO_6 samples, the critical angle has been found to be $\omega_c=0.34°\pm0.02°$ by a reflectivity measurement on an epitaxial film grown on a MgO(100) substrate in a separate experiment.[31] The corresponding penetration depth increases from 57 nm for $\omega=0.1°$ to 560 nm for $\omega=1.0°$.

For the sample obtained by the 1 min deposition [Fig. 3(a)], no diffraction features are found at incident angles larger than $\omega=0.2°$, which is consistent with a very thin film (~7 nm, Table I). A small diffraction peak at $2\theta=28.5°$ is observed for $\omega=0.2°$ (not shown) and it could be assigned as $SrO_2(101)$. However, there is no trace of the corresponding higher-intensity (110) peak of SrO_2, which makes the nature of this film uncertain.

Figure 4(a) compares the GIXRD spectra recorded with different incident angles for the samples obtained with 10 min [Fig. 3(b)], 30 min [Fig. 3(d)], and 60 min depositions [Fig. 3(e)]. For the thinner 10 min film (60 nm, Table I), two peaks at $2\theta=31.8°$ and $2\theta=45.7°$, corresponding respec-

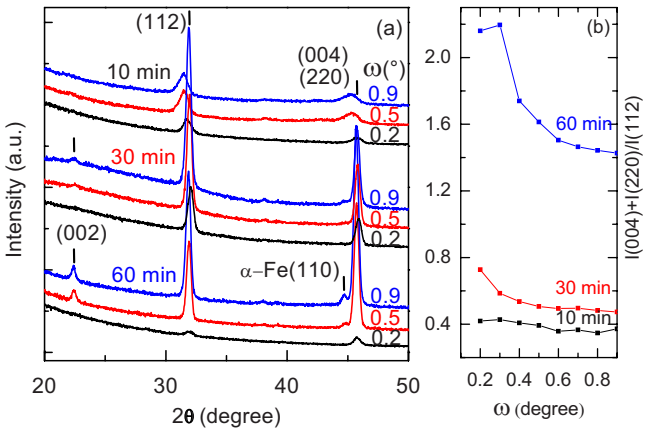

FIG. 4. (Color online) (a) GIXRD spectra collected at different incident angles $\omega=0.2°$, 0.5°, and 0.9° for Sr_2FeMoO_6 films grown on Si(100) for 10 min (top), 30 min (middle), and 60 min (bottom) deposition times. (b) Shows the corresponding intensity ratios of the (004)+(220) to (112) diffraction lines as a function of ω for the three films.

tively to the (112) and to the (004) and possibly (220) planes of Sr_2FeMoO_6, are observed at the surface of the film with $\omega=0.2°$. For higher incident angles of 0.5° and 0.9°, both diffraction features appear to shift to a lower 2θ angle. The width of the shifted (112) peak is unchanged while that of the shifted (004)+(220) feature becomes larger, suggesting the presence of a second phase of α-Fe with the (110) line at $2\theta=44.6°$.[23] The peak shift observed with increasing x-ray penetration depth into the film is consistent with the crystal lattice expansion of the film in the Sr_2FeMoO_6/Si interface region. This could be caused by a number of factors including different thermal expansion coefficients between Si (2.6×10^{-6} °C^{-1})[32] and Sr_2FeMoO_6 ($\sim9\times10^{-6}$ °C^{-1})[33] and local oxygen deficiencies due to the presence of native silicon oxide. For the thicker 30 min (114 nm, Table I) and 60 min films (268 nm, Table I), the same two Sr_2FeMoO_6 features for the (112) and (004)+(220) planes can be seen at $\omega=0.2°$ [Fig. 4(a)]. At higher incident angles, additional features attributed to Sr_2FeMoO_6(002) at $2\theta=22.4°$ and α-Fe(110) at $2\theta=44.6°$ become evident. The peak shifts for the 30 and 60 min films are less than that observed for the 10 min film. This is to be expected because the Sr_2FeMoO_6/Si interface region contributes a smaller percentage of the total diffraction signal for these thicker films.

In Fig. 4(b), we show the corresponding intensity ratio of the (004)+(220) to (112) lines as a function of the incident angle for the three films. For the 10 min film, this ratio (0.4 ± 0.1) is found to be close to the literature values for randomly oriented polycrystalline Sr_2FeMoO_6 powders (0.442). In contrast, the relative intensity ratio found for the 60 min film is much larger and decreases almost monotonically from 2.2 to 1.4, as the incident angle is increased from 0.3° to 0.9°. There is some scatter in the data below the critical angle $\omega_c=0.34°$. As the x rays should be reflected below ω_c, diffraction peaks below ω_c could be caused by imperfections in the sample surface (i.e., surface roughness) and artifacts of sample geometry, which also lead to the larger intensity scatter observed in this region. The intensity ratios for films grown with intermediate thicknesses (e.g., the 30 min film) follow a progression from the thin-film value (0.4) to the thicker-film value (1.4). This suggests that the grain orientation differs throughout the thickness of the film, where the Sr_2FeMoO_6 grains are more oriented at the film surface than the Sr_2FeMoO_6/Si interface. For the thicker films, we also see an increase in the intensity of the (002) peak at $2\theta=22.4°$.

These results indicate the preferential growth of (001) oriented Sr_2FeMoO_6 grains during long film depositions. Since the GIXRD data are convoluted with sample imperfections such as surface roughness and possible parasitic second phases (including metallic iron and $SrMoO_3$), it is difficult to estimate the extent of the preferential growth. The observed preferential oriented growth may be due to the influence of the laser plume on the Sr_2FeMoO_6 film growth during the PLD process, similar to the well-known ion-beam assisted deposition PLD technique, which has been used to introduce textured films on non-epitaxially matched substrates. Furthermore, developing the capability of synthesizing a high-quality oriented Sr_2FeMoO_6 film on Si will open up prospects for many potential applications. More detailed understanding of the mechanism behind this preferential growth will be presented in the future work as we investigate how the oriented growth depends on other variables including laser fluence, substrate-to-target distance, and gas environment during growth.

IV. CONCLUDING REMARKS

Using PLD, we have deposited and fully characterized Sr_2FeMoO_6 thin films on Si(100) substrates under different growth temperatures and deposition times. In contrast to the earlier work, nanocrystalline, single-phase Sr_2FeMoO_6 films could be obtained at a lower growth temperature (600–800 °C). Furthermore, the ferromagnetic films on Si(100) grown at 600 °C are found to be of high quality with saturation magnetic moments ($3.4\mu_B$ per formula unit at 77 K) that are comparable to the best Sr_2FeMoO_6 films epitaxially grown on lattice-matched substrates (such as $SrTiO_3$ and MgO) reported to date. As revealed by MFM, the as-grown film also exhibits micrometer-sized magnetic domains at room temperature, which are significantly larger than the grain sizes (200–250 nm). The low growth temperatures and the nonmagnetic nature of the Si substrate are useful for reducing chemical diffusion that may impair the magnetic properties of the Sr_2FeMoO_6 film. Moreover, by changing the x-ray incident beam angle, we also measure the diffraction patterns and determine the respective crystal structures of the film as a function of depth. For the as-grown Sr_2FeMoO_6 films thicker than 60 nm, a preferential orientation of the nanocrystals in the film is observed. The mechanism for the preferential oriented growth on Si, despite the lack of lattice matching due to the presence of native oxide, is unknown and additional studies will be conducted to further investigate this intriguing effect.

ACKNOWLEDGMENTS

This work was supported by the Natural Sciences and Engineering Research Council of Canada. We thank Dr. F.

Razavi, Dr. P. Dube, Dr. T. Hesjedal, and Dr. R. Engel-Herbert for their technical assistance and helpful discussions.

[1]S. A. Wolf, D. D. Awschalom, R. A. Buhrman, J. M. Daughton, S. Von Molnar, M. L. Roukes, A. Y. Chtchelkanova, and D. M. Treger, Science **294**, 1488 (2001).
[2]W. E. Pickett and J. S. Moodera, Phys. Today **54**, 39 (2001).
[3]C. Felser, G. H. Fecher, and B. Balke, Angew. Chem. **46**, 668 (2007).
[4]F. S. Galasso, *Structure, Properties and Preparation of Perovskite-type Compounds* (Pergamon, London, 1969).
[5]K.-I. Kobayashi, T. Kimura, H. Sawada, K. Terakura, and Y. Tokura, Nature **395**, 677 (1998).
[6]Y. Tomioka, T. Okuda, Y. Okimoto, R. Kumai, K.-I. Kobayashi, and Y. Tokura, Phys. Rev. B **61**, 422 (2000).
[7]Y.-H. Huang, H. Yamauchi, and M. Karppinen, Phys. Rev. B **74**, 174418 (2006).
[8]H. Q. Yin, J.-S. Zhou, J.-P. Zhou, R. Dass, J. T. McDevitt, and J. B. Goodenough, Appl. Phys. Lett. **75**, 2812 (1999).
[9]A. Di Trolio, R. Larciprete, A. M. Testa, D. Fiorani, P. Imperatori, S. Turchini, and N. Zema, J. Appl. Phys. **100**, 013907 (2006).
[10]T. Manako, M. Izumi, Y. Konishi, K.-I. Kobayashi, M. Kawasaki, and Y. Tokura, Appl. Phys. Lett. **74**, 2215 (1999).
[11]J. Navarro, L. I. Balcells, F. Sandiumenge, M. Bibes, A. Roig, B. Martinez, and J. Foncuberta, J. Phys.: Condens. Matter **13**, 8481 (2001).
[12]A. S. Ogale, S. B. Ogale, R. Ramesh, and T. Venkatesan, Appl. Phys. Lett. **75**, 537 (1999).
[13]T. Saha-Dasgupta and D. D. Sarma, Phys. Rev. B **64**, 064408 (2001).
[14]D. Niebieskikwiat, A. Caneiro, R. D. Sanchez, and J. Fontcuberta, Phys. Rev. B **64**, 180406 (2001).
[15]Y. Sui, X. Zhang, X. Wang, J. Cheng, W. Su, and J. Tang, J. Appl. Phys. **102**, 023903 (2007).
[16]M. Garcia-Hernandez, J. L. Martinez, M. J. Martinez-Lope, M. T. Casais, and J. A. Alonso, Phys. Rev. Lett. **86**, 2443 (2001).
[17]M. Besse, F. Pailloux, A. Barthelemy, K. Bouzehouane, A. Fert, J. Olivier, O. Durand, F. Wyczisk, R. Bisaro, and J.-P. Contour, J. Cryst. Growth **241**, 448 (2002).
[18]H. Asano, M. Osugi, Y. Kohara, D. Higashida, and M. Matsui, Jpn. J. Appl. Phys., Part 1 **40**, 4883 (2001).
[19]W. Zhong, W. Liu, C. T. Au, and Y. W. Du, Nanotechnology **17**, 250 (2006).
[20]M. Birkholz, *Thin Film Analysis by X-Ray Scattering* (Wiley-VCH Verlag GmbH & Co. KGaA, Wienheim, 2006).
[21]JCPDS Card No. 70–4092.
[22]JCPDS Card No. 70–2537.
[23]JCPDS Card No. 87–0721.
[24]JCPDS Card No. 52–1715.
[25]L. Y. Zhao, H. Jalili, N. Panjwani, T. Chan, Z. H. He, N. F. Heinig, and K. T. Leung, Electrochem. Solid-State Lett. **10**, K47 (2007).
[26]M. F. Doerner and S. Brennan, J. Appl. Phys. **63**, 126 (1988).
[27]M. F. Toney, T. C. Huang, S. Brennan, and Z. Rek, J. Mater. Res. **3**, 351 (1988).
[28]S. Debnath, P. Predecki, and R. Suryanarayanan, Pharm. Res. **21**, 149 (2004).
[29]T. C. Huang, Adv. X-Ray Anal. **33**, 91 (1990).
[30]K. Omote and J. Harada, Adv. X-Ray Anal. **43**, 223 (2000).
[31]H. Jalili, N. F. Heinig, and K. T. Leung (2008) (submitted).
[32]D. B. Chrisey and G. K. Hubler, *Pulsed Laser Deposition of Thin Films* (Wiley, New York, 1994).
[33]B. Garcia-Landa, C. Ritter, M. R. Ibarra, J. Blasco, P. A. Algarabel, R. Mahendiran, and J. Garcia, Solid State Commun. **110**, 435 (1999).